The importance of the shape of Cu2O nanocrystals on plasmon-enhanced oxygen evolution reaction in alkaline media

Tamazouzt Nait Saada, Liuqing Pang, Kilaparthi Sravan Kumar, André H.B. Dourado, Lucas Germano, Eduardo Vicentini, Ana P.L. Batista, Antonio G.S. de Oliveira-Filho, Franck Dumeignil, Sébastien Paul, et al.

The importance of the shape of Cu_2O Nanocrystals on plasmon-enhanced Oxygen Evolution Reaction in Alkaline Media

Tamazouzt Nait Saada,[1,2#] Liuqing Pang,[1#] Sravan Kumar,[1] André H.B. Dourado,[3] Lucas D. Germano,[3] Eduardo D. Vicentini,[4] Ana P.L. Batista,[4] Antonio G.S. de Oliveira-Filho,[4] Franck Dumeignil,[5] Sébastien Paul,[5] Robert Wojcieszak,[5] Sorin Melinte,[6] Georgiana Sandu,[6] Guido Petretto,[6] Gian-Marco Rignanese,[6] Adriano Henrique Braga,[3] Taissa F. Rosado,[7*] Dalila Meziane,[2] Rabah Boukherroub,[1] Susana I. Córdoba de Torresi,[3] Anderson G.M. da Silva,[7*] Sabine Szunerits[1*]

[1]*Univ. Lille, CNRS, Centrale Lille Univ. Polytechnique Hauts-de-France, UMR 8520 - IEMN, F-59000 Lille, France*

[2] *Laboratory of Applied Chemistry and Chemical Engineering (LCAGC), Université Mouloud Mammeri de Tizi Ouzou, Algeria*

[3]*Departamento de Química Fundamental, Instituto de Química, Universidade de São Paulo, Av. Prof. Lineu Prestes, 748, 05508-000, São Paulo, SP, Brazil*

[4]*Departamento de Química, Faculdade de Filosofia, Ciências e Letras de Ribeirão Preto, Universidade de São Paulo, 14040-901, Ribeirão Preto-SP, Brazil*

[5]*Univ. Lille, CNRS, Centrale Lille, Univ. Artois, UMR 8181 – UCCS – Unité de Catalyse et Chimie du Solide, F-59000 Lille, France*

[6]*Université catholique de Louvain, 1348 Louvain-la-Neuve, Belgium*

[7]*Departamento de Engenharia Química e de Materiais-DEQM, Pontifícia Universidade Católica do Rio de Janeiro (PUC-Rio), Rua Marquês de São Vicente, 225 - Gávea 22453-900 Rio de Janeiro - RJ -Brasil*

Abstract

# equal contributions
*To whom correspondence should be send to: agms@puc-rio.br (AGMS) or sabine.szunerits@univ-lille.fr (SS)

Cu_2O nanostructures of cubic and octahedral shape as well as decorated with gold nanoparticles were synthesized by a chemical process. The electrochemical activity of these nanostructures for the oxygen evolution reaction (OER) in alkaline media was assessed in the dark and under solar light irradiation. Electrodes modified with cubic-shaped Cu_2O and Cu_2O-Au nanostructures revealed both enhanced electrocatalytic OER activity over the octahedral-shaped ones, for which hydroxylation of the (111) surfaces might hinder the OER as supported by numerical computations. Illumination of Cu_2O nanostructures with solar light did not enhance the electrocatalytic OER. Cu_2O-Au nanostructures, however, showed improved OER activity with an overpotential of 200 mV (10 mA cm^{-2}) and Tafel slope of 97 mV dec^{-1}. The enhanced OER activity was ascribed to increased light absorption due to the plasmonic properties of Cu_2O-Au cubes.

Keywords: cuprous oxide; cubes; octahedra, gold nanoparticles, plasmon-enhanced electrocatalysis; oxygen evolution reaction; density functional theory

1. Introduction

The use of copper-based hybrid materials has largely advanced the field of electrocatalysis, as copper shows a large panel of redox properties, and various Cu-based hydrides have proven to be robust and of low-cost.[1-7] Cuprous oxide (Cu_2O) has a high absorption coefficient in the visible region making it well adapted for electrocatalytic [8-13] and photocatalytic redox reactions. [14, 15] Upon irradiation with photons of appropriate wavelength, electrons in the valence band can be promoted to the conduction band, resulting in photogenerated electrons and holes, used for photocatalytic driven redox reactions. As demonstrated by Xu et al.,[11] a three-dimensional Cu_2O-Cu hybrid electrode could overcome some of the limitations of Cu_2O for the oxygen evolution reaction (OER) in alkaline solution. These electrodes reached an overpotential of 250 mV and a Tafel slope of 67.52 mV dec^{-1} and showed a 50h durability at a current density of 10 mA cm^{-2}.

A different approach to accelerate the OER behavior of Cu_2O electrocatalysts is to increase the recombination time of electrons and holes via the presence of gold nanostructures onto the surface of Cu_2O.[9, 10] In these Cu_2O-Au hybrid materials, photoexcited electrons are shuttled from Cu_2O to the gold nanostructure, acting as electron sink, while the holes in the Cu_2O valence band remain free. Moreover, the localized surface plasmon resonance (LSPR) properties of gold nanostructures enables enhanced light absorption favorable for plasmon-enhanced photocatalysis. Pan et al. used these properties of Cu_2O-Au nanostructures for efficient degradation of methylene.[10]

In this work we investigated the electrocatalytic oxygen evolution reaction (OER) on five different interfaces (**Figure 1**): gold electrodes (noted as S1, and used as control), S1 coated with Cu_2O cubes (S2) or octahedra (S3), as well as gold nanoparticles-decorated Cu_2O (Cu_2O-Au) cubic (S4) and octahedral (S5) nanostructures. Indeed, cuprous oxide nanocrystals of cubic, octahedral, hexagonal shapes are reported in the literature.[16-19] We opted for comparing cubic to octahedral Cu_2O and Cu_2O-Au nanostructures, as octahedron-shaped Cu_2O nanostructured electrode having [20] facets have already been identified for having favorable properties in their applications such as lithium ion batteries.[21]. On the other hand, some of us[19] experimentally observed lately shape-dependent electrocatalytic glucose sensing performance of Cu_2O crystals in the order cubes > cuboctahedrons > octahedrons, with higher catalytic activity on the [20] facets by the stronger interaction with glucose.

The electrodes were formed by shape-directed solution synthesis of Cu_2O and Cu_2O-Au nanostructures followed by drop casting suspensions of the material onto gold thin film electrodes.

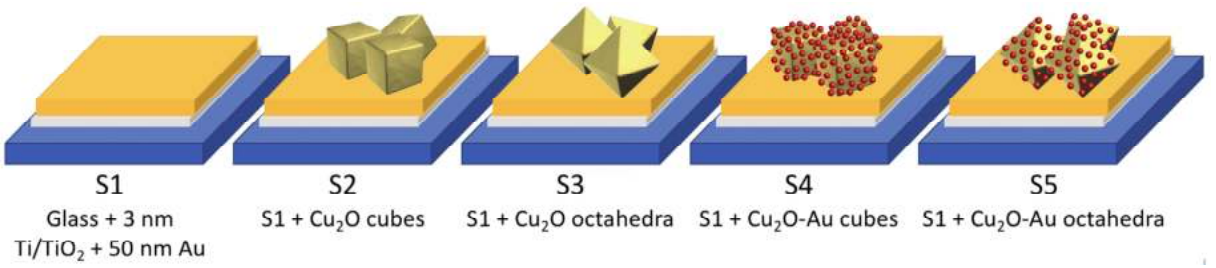

Figure 1. Schematic illustration of the five different electrode architectures employed for OER.

We highlight in this article that the morphology of Cu_2O nanocrystals has a strong influence on the electrocatalytic behavior for OER in basic medium: cubic shaped Cu_2O nanocrystals are more efficient than octahedral Cu_2O nanostructures. While the importance of Cu_2O crystal morphology has often been underlined in the context of catalysis,[22-24] it is not been considered in detail for the electrocatalytic oxygen evolution reaction. Using density function simulation, the lower catalytic activity of the octahedra nanostructures could be rationalized using kinetic considerations. It could be shown that the potential hydroxylation of the (111) surfaces of Cu_2O octahedra nanostructures hinder more strongly OER compared to cubic ones. We took this work further and show in addition that the addition of Au NPs onto these nanostructures allows their use for plasmon-enhanced electrocatalysis with cubic shaped Cu_2O-Au nanocrystals outperforming the others. Although plasmon-enhanced electrocatalytic activities using Au nanostructures on Cu_2O have been reported,[9, 10, 25-30] these studies did not investigate the structure-performance relationships of Cu_2O-Au electrocatalysts. It is, however, well accepted that exposed crystal facets can strongly affect the catalytic activity of Cu_2O nanostructures.[8, 31] Some of the present authors have demonstrated lately that selective electrochemical glucose oxidation occurs on Cu_2O cubes.[8] Here, we study systematically the influence of the morphology of Cu_2O-Au electrocatalyst on the efficiency of OER in basic medium to get a better understanding on how this parameter governs LSPR-mediated electrocatalytic processes. While it is well known that plasmon excitation of noble metal nanostructures on Cu_2O can (a) mediate/enhance chemical processes due to high light absorption at the metal–analyte interface, (b) form electron–hole pairs to promote charge-transfer processes and (c) locally rise the temperature giving an energy input for

electrochemical conversions, the question of how excited charge carriers generated during plasmon excitation of Au NPs affect charge transfer in Cu_2O of different shapes (cubic and octahedra) and consequently their catalytic activities remain lacking.

2. Results

2.1. Cubic and octahedra Cu_2O nanoparticles

Cu_2O nanostructures with cubic and octahedral morphology were obtained using $CuCl_2$ precursor, polyvinylpyrrolidone (PVP) as a shape-directing agent and sodium dodecyl sulfate (SDS) as a reducing agent under basic conditions ($NH_2OH \cdot HCl$). The synthesis of Cu_2O crystals was performed as follows:

$$2Cu(OH)_4^{2-}{}_{(aq)} + 2NH_2OH_{(aq)} \rightarrow Cu_2O(s) + N_{2(g)} + 5H_2O_{(l)} + 4OH^-{}_{(aq)}$$

Indeed, the formation of cubic and octahedral structures depends on the $NH_2OH \cdot HCl$ concentration, as this parameter influences the reaction kinetics and the growth rate along the [100] direction. We focused on the synthesis of Cu_2O cubes and octahedra displaying similar sizes (**Figure 2**).

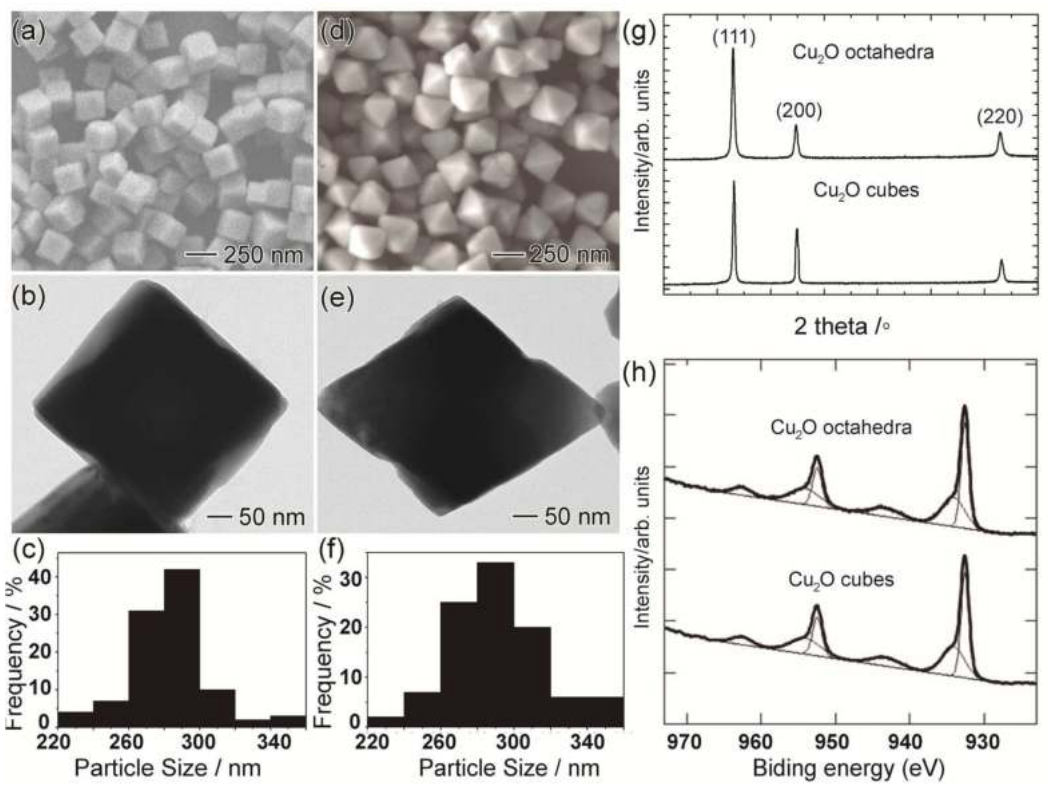

Figure 2. Characteristics of Cu_2O cubes and octahedra. (a and d) SEM and TEM (b and e) images of Cu_2O cubes (a and b) and Cu_2O octahedra (d and e). (c and f) histograms of particle

size distributions for cubes (c) and octahedra (f), respectively. (g) XRD patterns. (h) Cu 2p core level XPS spectra.

The size of the cubic Cu_2O crystals was determined from the SEM to be 298 ± 44 nm (**Figure 2a**), which is comparable to 302 ± 48 nm for the octahedral Cu_2O crystals (**Figure 2d**), which is in agreement with their histograms of particle size distributions crystals (**Figure 2c and 2f**). The XRD diffractograms (**Figure 2g**) of Cu_2O cubes and octahedra display (111), (200), and (220) crystallographic planes (JCPFS card number 05-0667). From XRD, on the basis of the Debye–Scherrer formula, the average grain size of the product along the [111] direction is about 44.2 and 55 nm for cubes and octahedral, respectively. The crystallite size and particle size differ hugely as indicated by XRD and TEM results. This can be explained as the calculation from XRD peaks gives the crystallite size not particle size, which based on the Scherrer formula (a single particle can consist of several crystalline subdomains). The relative intensity ratio between (200) and (111) crystal planes decreased with sharp variation, which agrees with the formation of Cu_2O cubes and octahedra bounded by (200) and (111) facets, respectively. The SAED pattern and phase-contrast HRTEM results (**Figure S1**) confirm the fact that the individual Cu_2O cubes and octahedra were single crystalline. The SAED patterns (**Figure S1 a-b**) for Cu_2O cubes and octahedra are composed of well-defined diffraction spots. These single crystal-like electron diffraction patterns indicate the presence of well-oriented Cu_2O NPs. The presence of lattice fringes corresponding to the [20] and [20] spacing of Cu_2O could also be observed for cubes and octahedra, respectively (**Figure S1 c-d**). XPS investigation of the Cu 2p region of both Cu_2O structures (**Figure 2h**) reveals bands at a binding energy of 932.5 and 952.4 eV corresponding to Cu(I) in Cu_2O, in accordance with literature reports[32] and XRD analysis. The additional band at 934.2 eV and 954.1 eV accounting for 17 at.% together with shake-up bands at 943.3 and 962.6 eV indicate the presence of some Cu^{2+} and surface CuO present.[32]

2.2. Synthesis and characterization of cubic and octahedra Cu_2O nanoparticles decorated with gold nanoparticles

Previous reports on the synthesis of Au NPs-decorated Cu_2O focused on using Au seeds to control the final shape of Cu_2O shells. Here, the Cu_2O cubes and octahedra were the templates for the formation Au NPs without the need of further surface modification step (**Figure 3a**). **Figure 3b-e** depicts SEM and TEM and images of the Cu_2O cubes and octahedra decorated

with Au NPs of about (5.0 ± 1.5 nm) in size as indicated by their histograms of particle distribution (Figure 3g-h)

The XRD patterns of Cu_2O-Au cubes and octahedra decorated (**Figure S2**) show that the peaks assigned to Cu_2O, (111), (200) and (220), remained unaffected after the deposition of Au NPs. The appearance of bands assigned to Au (111), (200) and (220) crystallographic planes could be clearly detected for both shapes.

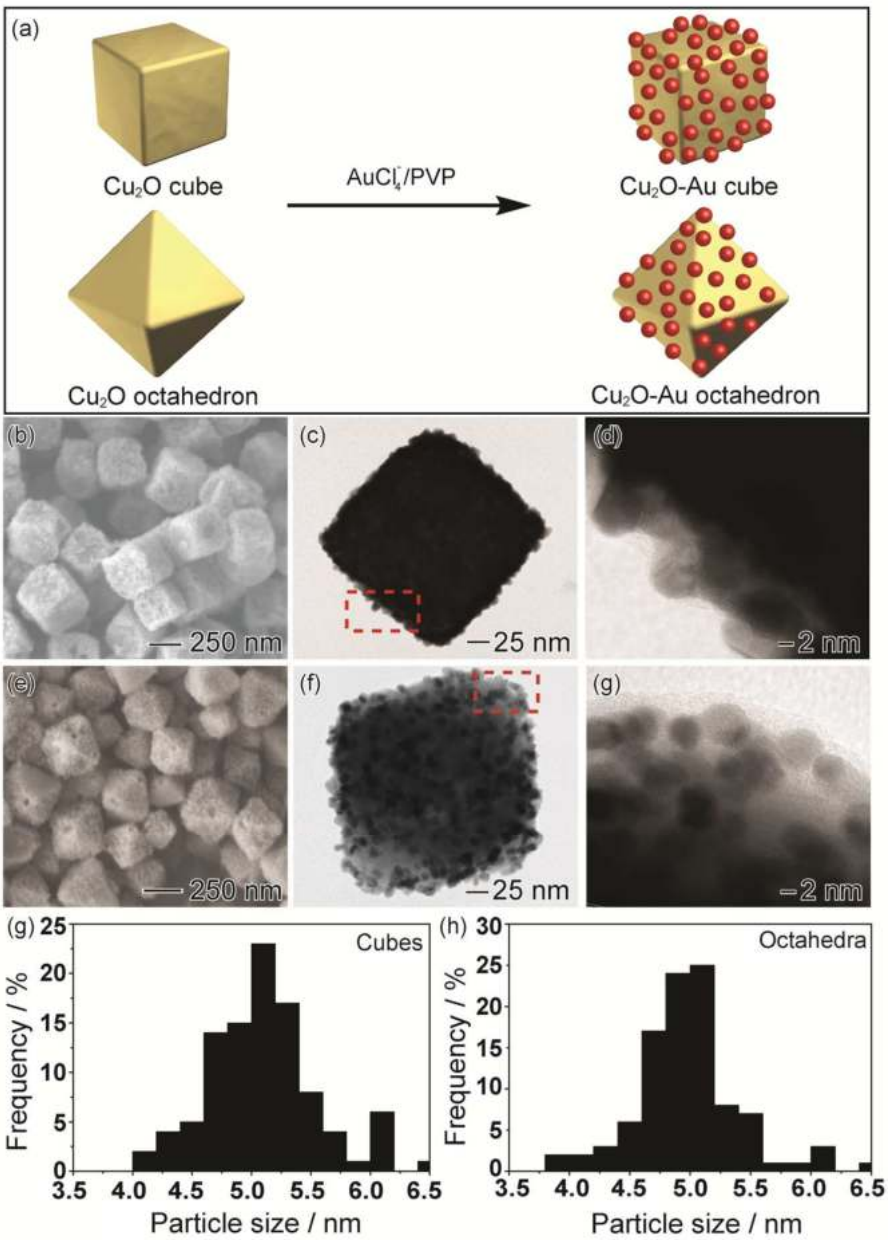

Figure 3. Cu_2O cubes and octahedra decorated with Au NPs on their surface. (a) Synthetic approach. (b, e) SEM images of Cu_2O-Au cubes and Cu_2O-Au octahedra. (c-d and f-g) TEM images of Cu_2O-Au cubes and Cu_2O-Au octahedra. (g-h) histograms of particle distribution.

Since the Au loading strongly influences plasmonic enhancements, the amount of Au loaded onto both Cu_2O nanostructures was determined by ICP-OES. Using the experimental condition as describe above, the atomic ratio of Au/Cu was determined as being 0.36±0.04 % for the cubic and 0.34±0.05% for the octahedral ones. The comparable Au loading will allow a correct comparison of the structures in the following.

Diffuse reflectance spectra were collected for Cu_2O cubes and octahedra to determinate their band gap energies (**Figure S3**). The determined band gap values were 2.75 and 2.94 eV for cubes and octahedra, respectively.

2.3. Oxygen evolution reaction

Five different electrodes S1-S5 (**Figure 1**) were investigated for their electrocatalytic activity in sodium hydroxide. In order to ensure correct and appropriate comparison among the electrodes, and in agreement with recommendations in recent literature,[33] the electrochemically active surface area (EASA) was determined by recording cyclic voltammograms where no faradic processes are observed (see SI, **Figure S4**). From the slope of the current density (*j*) *vs.* scan rate dependence, the electrode capacitance and the EASA values of S1-S5 (**Table S1**) were determined and used in the following.

The electrocatalytic activities of S1-S5 for OER in O_2-saturated 0.1 M NaOH are presented in **Figure 4a**. The gold electrode (S1) exhibits limited OER activity within the measured potential range. The onset of the OER on S2 is 1.46 V (*vs.* RHE) corresponding to an overpotential of η = 230 mV, comparable to IrO_2 (230 mV) [32, 34] and Cu_2O-Cu foam electrodes (250 mV).[11] An overpotential of 350 mV is required to reach 10 mA cm^{-2}. S3 has an OER onset potential at 1.61 V (*vs.* RHE) correlating to η = 470 mV at 10 mA cm^{-2}. The OER activity of S1-S4 (**Figure 4b**) showed to be independent on the mass loading of Cu_2O (**Table S2**). To benchmark the performance of S2, RuO_2 modified electrodes [35] of the same mass loading as Cu_2O (0.75 mg cm^{-2}) were prepared. An overpotential of 380 mV is required to reach 10 mA cm^{-2} (**Figure 4a**). The kinetics of the electrocatalytic OER reaction was evaluated by recording the corresponding Tafel plots (**Figure 4b**). Tafel slopes of 116 mV/decade (S2) and 135 mV/decade (S3) were determined. Decoration of Au nanoparticles onto Cu_2O does not show any further improvement of the OER reaction (**Table 1a**). The results indicated that the cubic-shaped Cu_2O nanostructures were more active than the octahedral ones. The Cu_2O and Cu_2O-Au cubes have OER activity comparable and even superior to a large range of other metallic and non-metallic OER catalysts (**Table 1b**).

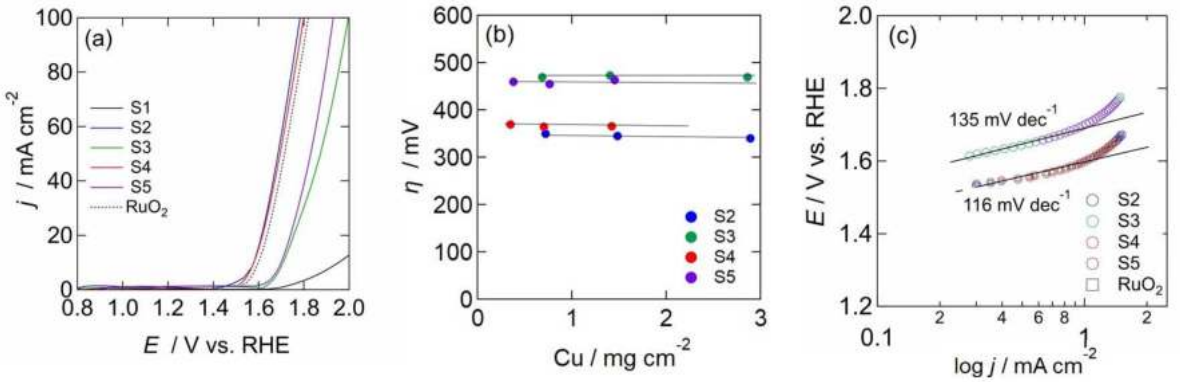

Figure 4. Oxygen evolution reaction (OER) under basic conditions. (a) LSV in O_2-deaerated NaOH (0.1 M) of S1 (black), S2 (blue), S3 (green), S4 (red) and S5 (violet), scan rate of 25 mV s^{-1}. Electrode coated with RuO_2 (0.75 mg cm^{-2}) as control (dotted line) (b) Influence of Cu mass on overpotential at 10 mA cm^{-2}. (c) Tafel plots of S1 (black), S2 (blue), S3 (green), S4 (red) and S5 (violet). Squares are for electrode coated with RuO_2 (0.75 mg cm^{-2}) as control.

Table 1: **OER activity**: (a) Tafel slopes of S2-S5 and (b) Comparison of electrocatalytic activity of some reported Cu-based nonprecious OER electrocatalysts in alkaline media.

(a)

Interface	**η / mV (10 mA cm^{-2})**	**Tafel slope (mV/decade)**
S2	350	116
S3	470	135
S4	370	116
S5	460	135
RuO_2 (0.7 mg cm^{-2})	380	116

(b)

Catalyst	**η / mV (10 mA cm^{-2})**	**Tafel slope (mV/decade)**	**Reference**
Cu-N-C/graphene	770	n.a.	[36]
AuNi- Cu_2O	601	64.8	[3]
$CuFe_2O_4$ spinel nanofibers	490	94	[37]
Cu_2O-Cu foams	350	67.5	[11]
Cu_2O@C nanoparticles	330	63	[38]
Cu_2O and Cu_2O-Au nanocubes on gold electrodes	350	116	This work
Cu/Cu_2O/CuO	290	64	[39]
Cu_2O-Au nanocubes under solar light irradiation	200	97	This work

These observations agree with our theoretical results obtained by quantum chemical calculations (**Figure S5)** with the GFN0-xTB tight binding method, for model clusters of Cu_2O nanoparticles and Cu_2O-Au NPs[40]. To better understand the experimental results, density functional (DFT) simulations were also performed. In order to mimic the OER for cubic and octahedral nanostructures, Cu_2O slabs with (100) and (111) surfaces were considered, respectively, both without and with hydroxyl groups (the former being thermodynamically more stable for the (111) surface, and the one with 100% OH coverage for the (100) one, **Figures S6** and **S7**). Following a methodology developed by Nørskov et al., a computational hydrogen electrode was used to estimate the intermediate energy of each of the proton-coupled electron transfer steps as a function of the electrochemical potential.[24]. Contrarily to the observed experimental trends, the Nørskov model predicts a lower overpotential for the (111) surfaces, as reported in **Figure 5**. This holds for the pristine surfaces (without hydroxyl groups) as well as for the hydroxylated ones (see SI for more details). While it may happen that this model cannot fully account for the experimental results [25] we believe that, here, the latter may still be rationalized by considering the interaction of the adsorbates with other atoms potentially present on the surface during the intermediate steps.

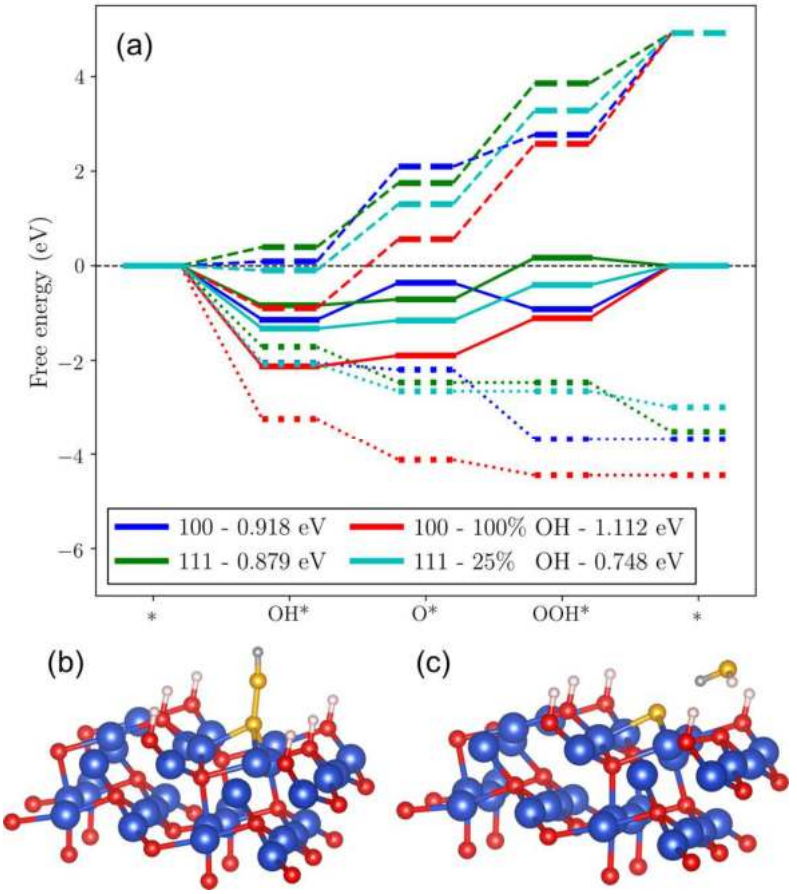

Figure 5. Calculations for OER for cubic and octahedral nanostructures. (a) Free energies of OER intermediates for (100) and (111) oriented Cu_2O surfaces: 1.23 V vs. RHE (solid line), 0 V vs. RHE (dashed line), dotted line for the minimum potential. Values indicate the calculated overpotential. Blue and green (red, cyan) lines represent the energies for surfaces without (with) hydroxyl groups (the coverages are 25% and 100% for the (111) and (100) surfaces, respectively, see SI for more details). Side view of the (111) surface for the OOH* adsorbate with full H coverage. The initial configuration (b) and the relaxed structure (c), with the formation of an H_2O on top of the surface. Cu (blue), Oxygen (red), hydrogen (white). Yellow and gray spheres represent the O and H atoms for the adsorbed OOH* group.

We observed that the hydroxyl of the OOH* group is only loosely bound in the case of the (111) surface. As soon as an H atom gets adsorbed on an O atom close enough to the active site, it gets captured by the hydroxyl of the OOH* group to form an H_2O molecule which detaches from the surface. This prevents the subsequent steps and hinders the OER. In addition, when performing molecular dynamics simulations at room temperature to follow the evolution of the adsorbed OOH*, it was found that the latter tends to move quite easily from

one Cu adsorption site to another. This makes the H_2O molecule detachment more likely to happen. In contrast, in the case of the (100) surface, none of these two mechanisms show up. Hence, its activity is quite independent of the hydroxylation conditions. The lower activity of the octahedra nanostructures could be thus explained by the potential hydroxylation of the (111) surfaces that hinders the OER. While purely thermodynamics arguments lead to predictions in contradiction with experimental results, kinetic considerations pondering the environment reconcile both pictures.

2.4. Oxygen evolution reaction upon light illumination

The *p*-type Cu_2O semiconductor displays a broad absorption from 500-800 nm, a region which accounts for 42-43% of the total sun light irradiation. Gold-based nanoparticles, on the other hand, exhibit narrow absorption bands with spherical colloidal gold particles having absorbance maxima between 515-570 nm.[10] Integration of Au nanoparticles onto Cu_2O is expected to increase light absorption, form LSPR excited hot charge carriers and might work as electron sink of electrons generated in Cu_2O.[10].

The UV-vis absorption spectra of S2-S5 (**Figure 6a**) show a broad absorption between 450-680 nm with a maximal absorption at around 561 nm. In contrast to S2 (Cu_2O only) the presence of Au nanoparticles on Cu_2O (S4) exhibits a red shift in its maximum to 606 nm with an intense absorption between 450-760 nm. The LSPR band of the Au nanostructures overlaps with the absorption spectrum of Cu_2O. S3 and S5 display sharper UV-vis signatures with absorption maxima at about 566 nm (S3) and 570 nm (S5). The presence of Au NPs in S3 and S4 is largely overlapped by the Cu_2O absorption band. However, closer inspection of the UV-vis spectra for S4 and S5 shows a shoulder at 518 nm, characteristics of Au nanospheres of 12 nm in diameter.

Figure 6b depicts the linear sweep voltammograms of S1-S5 when irradiated with a 150 W arc lamp at a power density of 1.3 sun (180 mW cm^{-2}). No change in OER behavior was observed for S1-S3. This indicates most likely that the generated hole-electron pairs in Cu_2O are recombining faster, making unavailable the holes for water oxidation. The situation is different in the case of S4 and S5. Solar-light illumination shifts the OER onset potential to 1.39 V (*vs.* RHE) for S4 and 1.52 V (*vs.* RHE) for S5 (**Figure 6b**) corresponding to an overpotential of 200 mV to reach 10 mA cm^{-2} for S4 and 350 mV for S5. The Tafel plots (**Figure 6c**) indicate an enhancement in the OER kinetics for both interfaces with Tafel slopes of 97 mV dec^{-1}. To be noted, such light density does not result in rise in the solution

temperature even when illuminated for more than 30 min (**Figure S8a**). This experiment concludes that heating effects and near-field enhancement effects can be excluded. Furthermore, illumination with a laser at 980 nm using the same power density (180 mW cm^{-2}) does not yield any change in catalytic activity (**Figure S8b-c**). This wavelength dependence is a clear evidence of the generation of surface plasmons. The acceleration of OER oxidation depends on the incident light power density (**Figure S9a**), while no increase in the current density was recorded upon irradiation at 980 nm. In a last control, we deposited commercially available Au NPs of 10 nm on S1 (S1+Au NPs) and investigated the OER with and without light solar-light irradiation (**Figure S9b**). Without the presence of Cu_2O no significant electrocatalytic activity was observed.

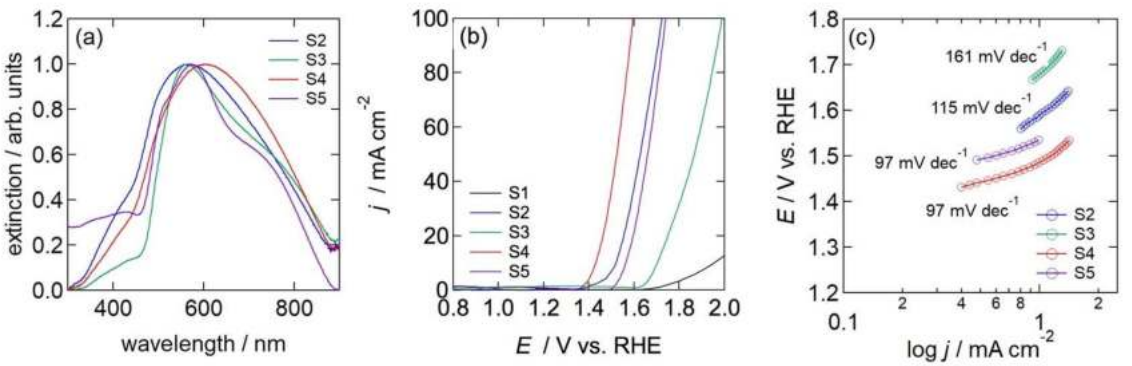

Figure 6. Oxygen evolution reaction (OER) under irradiation. (a) UV-vis spectra of S2-S5. (b) LSV in O_2-deaerated NaOH (0.1 M) of S1 (black), S2 (blue), S3 (green), S4 (red) and S5 (violet) under illumination (150 W arc lamp, power density 180 mW cm^{-2}, scan rate = 25 mV s^{-1}. (c) Tafel plots of S2 (blue), S3 (green), S4 (red) and S5 (violet) under illumination.

Assuming that the conduction band of Cu_2O is situated below that of the LSPR state of Au, [10, 41] following mechanism was concluded: under light excitation, charge separation is occurring in Cu_2O forming electron-hole pairs. The photogenerated electrons are shuttled to Au (**Figure 7a**). The resultant electron-deficient Cu_2O cubes due to the Au NPs electron sink, oxidize water under basic conditions to oxygen. The current density profile abruptly changes indeed upon laser irradiation (**Figure 7b)** when S4 is biased at 1.44 V (*vs.* RHE).

The conductivity of S4 without and under light illumination was in addition demonstrated using electrochemical impedance spectroscopy (EIS) in 0.1 M NaOH (**see SI, Figure S10**). According to previous literature reports, the high-frequency response is assigned to the

intrinsic resistance of the catalyst while the low-frequency response is assigned to charge transfer process (R_{ct}) of oxygen at the catalyst interface [42]. The R_{ct} of S4 under solar light illumination is smaller than when recorded in the dark, and favourable for enhanced electrocatalytic activity.

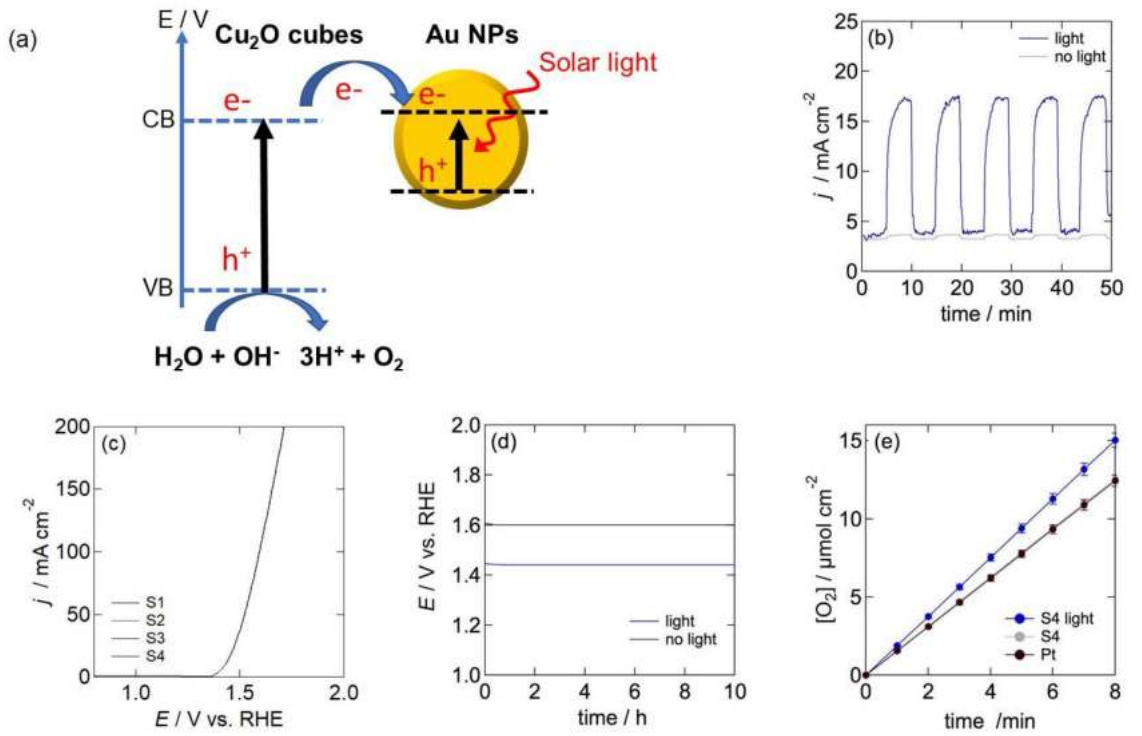

Figure 7. Mechanistic considerations for OER on S4. (a) Mechanism of enhance OER. (b) Current density - time curves at E = 1.44 V (vs. RHE) under light illumination for repeated intervals (5 times) for 10 min (blue) and with no illumination (gray) for S4. (c) LSV curves in 0.1 M NaOH 25 mV $s^{-1)}$ in dark. (d) Stability test (j = 10 mA cm^{-2}) under light illumination (blue) and in dark (gray). (e) Oxygen conversion efficiency at 1.50 V in 0.1 M NaOH with (blue) and without (grey) light irradiation (symbols). Theoretical efficiency (lines).

The OER is reproducible (**Figure 7c**). The long-term stability of S4 (**Figure 7d)** assessed at j = 10 mA cm^{-2} indicate stability for at least 10 h of continuous OER. Up to 14 µmol cm^{-2} O_2 was formed after irradiation for 8 min, which represents a 3-fold enhancement compared to S4 without activation (**Figure 7e**). To support further the material stability after 10 h continuous OER, SEM images of the Cu_2O-Au nanocrystals were performed as well as XRD

analysis (**Figure S11**). The octahedra Cu2O nanostructure remains clearly visible with the XRD patterns of Cu_2O and Au being still visible

3. Conclusion

In conclusion, Cu_2O cubes decorated with gold nanostructures (Cu_2O-Au) show enhanced OER activity in alkaline media under solar light illumination. The enhanced OER activity was ascribed to increased light absorption due to the plasmonic properties of Cu_2O-Au cubes. Indeed, illumination Cu_2O nanostructures with solar light did not enhance the electrocatalytic OER. The Cu_2O-Au nanostructures need an overpotential of 200 mV to reach 10 mA cm^{-2} with a Tafel constant of 97 mV dec^{-1}. Furthermore, cubic Cu_2O structures were more active than octahedral ones. Numerical computations suggest that the lower activity of the Cu_2O octahedra nanostructures could be explained by the potential hydroxylation of the (111) surfaces, that hinders the OER. The Cu_2O-Au, when deposited on gold thin film electrodes, sustains the oxygen evolution reaction for several hours without surface poisoning or electrode degradation.

Supporting Information Available: S1: Characterization. S2 Electrochemical experiments Table S1. Determined capacitance values for S1-S5 from Figure S2 together with calculated EASA values. Table S2. ICP-OES (inductively coupled plasma - optical emission spectrometry) analysis of the material loading on S1. Figure S1. SEAD patterns and (c-d) HRTEM imagens for Cu_2O cubes octahedra. Figure S2. X-ray diffraction (XRD) patterns for Cu_2O-Au cubes and Cu_2O-Au octahedra. Figure S3. Determination of the optical bandgap of the nanostructures using diffuse reflectance for (a) Cu_2O cubes (blue), (b) Cu_2O octahedra (green), (c) Cu_2O-Au cubes (red) and (d) Cu_2O-Au octahedra (violet). Figure S4. Determination of electrochemical active surface area (EASA). (a-e) Cyclic voltammograms in 0.1 M NaOH at different scan rates for S1-Au, S2-Au/Cu_2O cubes, S3-Au/Cu_2O octahedra, S4-Au/Cu_2O-Au cubes, S5-Au/Cu_2O-Au octahedra. (f) Current density *vs.* scan rate of S1-S5. Figure S5. Mulliken atomic partial charges calculated with the GFN0-xTB tight binding method for (a) $(Cu_2O)_{63}Au_4$ cube and (b) $(Cu_2O)_{63}Au_4$ octahedron. The scale bars indicate the electronic charge in terms of elementary charge *e*. Figure S6. Relaxed geometries of the Cu_2O (100) and (111) surfaces used in density functional theory study. Figure S7. Stability as a function of the potential with different amounts of hydrogen atoms adsorbed for (100) and (111) surfaces. Figure S8. (a) Change of solution temperature of S4 (red) and S5 (violet) when irradiated with a 150 W arc lamp at a power density of 1.3 sun (180 mW cm^{-2}) (full line) or with a laser at 980 nm (180 mW cm^{-2}) (dotted line) for 30 min. (b) Linear sweep voltammograms at 980 nm (180 mW cm^{-2}) in O_2-deaerated NaOH (0.1 M) of S1 (black), S4-Au/Cu_2O-Au cubes (red) and S5-Au/Cu_2O-Au octahedra (violet), scan rate of 25 mV s^{-1}. (c) Tafel plots of S4 (red) and S5 (violet) under illumination. Figure S9. (a) Influence of solar

light intensity and intensity of a 980 nm laser on the OER overpotential determined on S4 in O_2-deaerated NaOH (0.1 M). (b) Linear sweep voltammograms with and without solar-light irradiation (180 mW cm^{-2}) in O_2-deaerated NaOH (0.1 M) of S1+Au NPs (10 nm). **Figure S10.** EIS Nyquist plots of S4 at open circuit potential in 0.1 M NaOH without and with solar light illumination.

Acknowledgements

Financial support from the Centre National de la Recherche Scientifique (CNRS), the University of Lille and the Hauts-de-France region *via* the dispositif *STIMulE* (Soutien aux travaux interdisciplinaires 2019) is acknowledged. This work was also supported by the São Paulo Research Foundation (FAPESP) (grant number 2015/26308-7) and Fundação de Amparo à Pesquisa do Estado do Rio de Janeiro (FAPERJ). S.I.C.T. and A.G.M.S. thank CNPq and FAPERJ for their research fellowships. A.G.M.S. and L.D.G. thank FAPESP for their fellowship (grant numbers FAPESP 2017/12407- 9, 2018/25567-7, and 2018/22845-6).

4. Experimental Section

4.1. Materials

Sodium dodecyl sulfate (SDS, ≥90%, VETEC), polyvinylpyrrolidone (PVP, Sigma-Aldrich, M.W. 55.000 g mol^{-1}), hydroxylamine hydrochloride ($NH_2OH.HCl$, ≥99%, Merck), sodium hydroxide (NaOH, ≥97%, Synth), γ–butyrolactone ($C_4H_6O_2$, Sigma-Aldrich, 99%,) copper (II) chloride dihydrate ($CuCl_2.2H_2O$, ≥99%, Sigma-Aldrich), tetrachloroauric acid ($HAuCl_4.3H_2O$, ≥99%, Sigma-Aldrich), gold nanoparticles (10 nm) were used as received.

4.2. Synthesis of Cu_2O cubes

1 g of sodium dodecyl sulfate (SDS) and 1 mL of $CuCl_2$(aq) (0.1 M) were added to 94 mL of water and mixed until the complete dissolution. Then, 2.5 mL of $NH_2OH.HCl$(aq) (0.2 M) and 2.5 mL NaOH(aq) (1 M) were added sequentially. The resulting mixture was mixed under magnetic stirring (200 rpm) for 2 h at room temperature. After this time, the supernatant was removed by centrifugation for 10 min at 7.800 rpm and the solid was suspended in 100 mL of PVP aqueous solution (0.1 wt.%) for the synthesis of bimetallic structures after addition of $HAuCl_4$(aq).

4.3. Synthesis of Cu_2O octahedra

1 g of SDS and 1 mL of $CuCl_2$(aq) (0.1 M) were added to 88 mL of water and mixed until the complete dissolution. Then, 8.5 mL of $NH_2OH.HCl$(aq) (0.2 M) and 2.5 mL NaOH(aq) (1 M)

were added sequentially. The resulting mixture was mixed under magnetic stirring (200 rpm) for 2 h. The supernatant was removed by centrifugation for 10 min at 7.800 rpm and the solid was suspended in 100 mL of PVD (0.1 wt.% in water).

4.4. Synthesis of Cu_2O-Au nanomaterials

A suspension of 50 mL of Cu_2O cubes or octahedra in PVP (0.1 wt.%) was stirred at 90 °C for 10 min. Then 7.5 mL of $HAuCl_4$ (0.375 M) was added and the mixture was kept for 30 min at 90 °C. The formed bimetallic nanomaterial was washed twice with 50 mL of γ–butyrolactone, ethanol, and water by successive rounds of centrifugation at 7.800 rpm for 10 min and removal of the supernatant. The particles were then suspended in 1 mL water.

4.5. Computational methods

Density functional theory and molecular dynamics computations. Spin polarized DFT calculations were performed with the Vienna Ab-initio Simulation Package (VASP) using a plane-wave basis set and the projector augmented wave (PAW) method[26,27]. The calculations were carried out at the PBE-D3(BJ)+U level of theory,[28-30] with a U–j value of 3.6 eV.[31] The energy cutoff for the plane waves was set to 400 eV. All the energies were obtained after the system has been relaxed until all the forces were below 0.005 eV/Å. The lattice parameter (4.249 Å) has been determined from the calculation of a bulk Cu_2O with a 6×6×6 *k*-points grid. All the surfaces considered were roughly 12 Å thick with a vacuum of at least 15 Å. During relaxation, the bottom four and five layers were kept fix for (100) and (111) slabs, respectively. The (100) surface was modeled with a (1×1) pattern with oxygen terminations, which has been shown to be the most stable under oxygen rich conditions[32-33]. A 2×2×1 supercell was used when considering the adsorbates, sampling the Brillouin zone with a 3×3×1 *k*-points grid. For the OER process, the initial step is simulated by removing one O atom from the original surface and that region is considered as the active site for the remaining steps. The (111) surface was modeled with a (1×1) pattern, where reconstruction of the top layer Cu_{CUS} was allowed[34]. A 2×2×1 supercell was used with a 2×2×1 *k*-points sampling. The adsorption site considered is the reconstructed Cu_{CUS}. Dipole-correction option incorporated in the VASP code[35,36] was used to counterbalance the errors associated with the surface dipole moment in the periodic calculations. Molecular dynamics simulations of the surfaces were performed with a Nosé-Hoover thermostat at 300 K for 1 ps.

Cluster modeling. Following previous works,[37] to approach the Cu_2O nanocrystals, a cluster model of 189 atoms, $(Cu_2O)_{63}$, was employed. The effect of the gold deposition on the Cu_2O

nanoparticles was considered by allowing an Au_4 cluster to relax over each one of the explored Cu_2O surfaces. Toward this end, a computational study employing the GFN0-xTB method,[37,38] as implemented in the xTB program (version 6.2.2), was adopted. The density of states (DOS) of the four $(Cu_2O)_{63}$ and $(Cu_2O)_{63}Au_4$ systems (cubes and octahedron) were obtained from the xTB orbital energies using Gaussian smearing with a width of 0.05 eV.

References

[1] M.B. Gawande, A. Goswami, F.-X. Felpin, T. Asefa, X. Huang, R. Silva, X. Zou, R. Zboril, R.S. Varma, Cu and Cu-Based Nanoparticles: Synthesis and Applications in Catalysis, Chem.Rev., 116 (2016) 3722−3811

[2] H. Lee, X. Wu, L. Sun, Copper-based homogeneous and heterogeneous catalysts for electrochemical water oxidation, Nanoscale 12 (2020) 4187-4218

[3] H. Gong, S. Lu, P. Strasser, R. Yang, Highly efficient AuNi-Cu2O electrocatalysts for the oxygen reduction and evolution reactions: Important role of interaction between Au and Ni engineered by leaching of Cu2O., Electrochim. Acta, 283 (2018) 1411-1417.

[4] T. Li, H. Wei, T. Liu, G. Zheng, S. Liu, J.-L. Luo, Achieving Efficient CO2 Electrochemical Reduction on Tunable In(OH)3-Coupled Cu2O-Derived Hybrid Catalysts, ACS Appl. Mater. Interfaces 11 (2019) 22346–22351.

[5] H. Manisha, P.D. Priya Swetha, Y.-B. Shim, K.S. Prasad, Microwave Assisted Synthesis of Hybrid Cu2O Microcubes for Photocatalysis and Electrocatalysis, Mat. Today: Proceedings, 5 (2018) 16390-16393.

[6] X. Tan, C. Yu, C. Zhao, H. Huang, X. Yao, X. Han, W. Guo, S. Cui, H. Huang, J. Qiu, Restructuring of Cu2O to Cu2O@Cu-Metal–Organic Frameworks for Selective Electrochemical Reduction of CO2, ACS Appl. Mater. Interfaces, 11 (2019) 9904–9910.

[7] Z. Zhou, X. Li, Q. Li, Y. Zhao, H. Pang, Copper-based materials as highly active electocatalysts for the oxygen evolution reaction, Mater. Today Chem., 11 (2019) 169-196.

[8] A.H.B. Dourado, A.G.M. da Silviz, F.A.C. Pastrian, R.L. Munhos, A.D. de Lima Batista, A.G.S. de Oloveria-Filho, J. Quiroz, D.C. deOliveira, P.H.C. Camargo, S.I. Dordoba de Toeressi, In situ FTIR insights into the electrooxidaiton mechanism of glucose as a funciton of the surface facets of Cu20-based electrocatalytic sensors, J. Catal., 375 (2019) 95.

[9] X.-W. Liu, Selective growth of Au nanoaprticles on (111) facets of Cu2O microcrystals with an enhanced electrocatalytic property, Langmuir, 27 (2011) 9100-9104.

[10] Y. Pan, S. Deng, L. Polavarapu, N. Gao, P. Yuan, C.H. Sow, Q.-H. Xu, Plamson-Enhanced photocatalytic proeprties of Cu2O nanowire-Au nanoparticle assemblies, Langmuir, 28 (2012) 12304.

[11] H. Xu, J.-X. Feng, Y.-X. Tong, G.-R. Li, Cu2O-Cu hybrid foams as high-performance electrocatalyst for oxygen evolution reaction in alcaline media, ACS Catal., 7 (2017) 986-991.

[12] S. Ikeda, T. Takata, T. Kondo, G. Hitoki, M. Hara, J. Kondo, K. Domen, H. Hosono, H. Kawazoe, A. Tanaka, Mechano-catalytic overall water splitting, Chem. Commun., 20 (1998) 2185.

[13] R.M. Arán-Ais, R. Rizo, P. Grosse, G. Algara-Siller, K. Dembélé, M. Plodinec, T. Lunkenbein, S.W. Chee, B.R. Cuenya, Imaging electrochemically synthesized Cu2O cubes and their morphological evolution under conditions relevant to CO2 electroreduction, Nat. Commun., 11 (2020) 3489.

[14] C.Y. Toe, Z. Zheng, H. Wu, J. Scott, a. R., Y.H. Ng, Photocorrosion of Cuprous Oxide in Hydrogen Production: Rationalising Self-Oxidation or Self-Reduction, Angew. Chem. Int. Ed., 57 (2018) 13613-13617.

[15] C.Y. Toe, J. Scott, R. Amal, Y.H. Ng, Recent advances in suppressing the photocorrosion of cuprous oxide for photocatalytic and photoelectrochemical energy conversion, J. Photochem. Photobiol., DOI (2019) 191-211.
[16] M.L. Bhaisare, M.S. Kahn, S. Pandey, G. Geddad, H.F. Wu, Shape-oriented photodynamic therapy of cuprous oxide (Cu2O) nanocrystals for cancer treatment, RSC Advances, 7 (2017) 23607-23614
[17] M.H. Huang, C.-Y. Chiu, Achieving polyhedral nanocrystal growth with systematic shape control, J. Mater. Chem. A, 1 (2013) 8081-8092
[18] A. Radi, D. Pradhan, Y. Sohn, K.T. Leung, Nanoscale Shape and Size Control of Cubic, Cuboctahedral, and Octahedral Cu−Cu2O Core−Shell Nanoparticles on Si(100) by One-Step, Templateless, Capping-Agent-Free Electrodeposition, ACS Nano, 4 (2010) 1553–1560.
[19] F.A.C. Pastrián, A.G.M. da Silva, A.H.B. Dourado, A.P. de Lima Batista, A.G.S. de Oliveira-Filho, J. Quiroz, D. de Oliveira, P.H.C. Camargo, S.I. Córdoba de Torresi, Why Could the Nature of Surface Facets Lead to Differences in the Activity and Stability of Cu2O-Based Electrocatalytic Sensors?, ACS Catal.,, 6265–6272 (2018).
[20] G.-B.S.P.f.O.-C.O.A. Detection., Nekrasov N1, Kireev D2, Emelianov A1, B. I3, A. information, S. Toxins, 11(10), D. 10.3390/toxins11100550, DOI.
[21] M.-C. Kim, S.J. Kim, S.-B. Han, D.-H. Kwak, E.-T. Hwang, D.-M. Kim, G.-H. Lee, H.-S. Choe, K.-W. Park, Cubic and octahedral Cu2O nanostructures as anodes for lithium-ion batteries, J. Mater. Chem. A, 3 (2015) 23003-23010
[22] A.K. Mishra, D. Pradhan, Morphology Controlled Solution-Based Synthesis of Cu2O Crystals for the Facets-Dependent Catalytic Reduction of Highly Toxic Aqueous Cr(VI), Cryst. Growth Des., 17 (2016) 3688–3698.
[23] L.D. MouraTorquato, F.A.C. Pastrian, J.A. Lima Perini, K. Irikura, A.P.L. Batistad, d.O.-F.A.G. S., S.I. Córdoba de Torresi, M.V. Boldrin Zanoni, Relation between the nature of the surface facets and the reactivity of Cu2O nanostructures anchored on TiO2NT@PDA electrodes in the photoelectrocatalytic conversion of CO2 to methanol, App. Catal. B, 261 (2020) 118221.
[24] H. Bao, Z. Zhang, Q. Hua, W. Huang, Compositions, Structures, and Catalytic Activities of CeO2@Cu2O Nanocomposites Prepared by the Template-Assisted Method, Langmuir, 30 (2014) 6427–6436.
[25] D. Chen, R. Zhang, R. Wang, L. Dal Negro, S.D. Minteer, Gold nanofiber-based electrode for plasmon-enhanced electrocatalysis, J. Electrochem. Soc., 163 (2016) H1132-H1135.
[26] S. Mukherjee, L.N. Zhou, A.M. Good man, N. Large, C. Ayala-Orozco, Y. Zhang, P. Nordlander, N.J. Halas, Hot-Electron-induced Dissociation of H2 on Gold nanoaprticesl supported on SiO2, J. Am. Chem. Soc., 136 (2014) 64-67.
[27] C. Wang, X.-G. Nie, Y. Shi, Y. Zhou, J.-J. Xu, X.-H. Xia, H.-Y. Chen, Direct Plamson-accelerated electrochemial reaciton on gold nanoparticles, ACS Nano, 11 (2017) 5897-5907.
[28] C. Wang, X.-P. Zhao, Q.-Y. Xu, X.-G. Nie, M.R. Younis, W.-Y. Liu, X.-H. Xia, Importance of Hot Spots in gold nanostructures on direct plasmon-enhance electrochemistry, ACS App. Nano Mater., 1 (2018) 5805-5811.
[29] J. Xu, P. Gu, D.J.S. Birch, Y. Chen, Plasmon-Promoted electrochemical oxygen evaolution catalysis from gold decorarted MnO2 nanosheets under green light, Adv. Funct. Mater., 28 (2018) 1801573.
[30] L. Yan, F. Wang, S. Meng, Quantum Mode Selectivity of Plasmon-Induced Water Splitting on Gold Nanoparticles, ACS Nano, 10 (2016) 5452-5458.
[31] Y. Kwon, A. Soon, H. Han, H. Lee, Shape effects of cuprous oxide particles on stability in water and photocatalytic water splitting, J. Mater. Chem. A, 3 (2015) 156.
[32] D. Tahir, S. Tougaard, electronic and optical properties of Cu, CuO and Cu_2O studies by electron spectrosopy, J. Phys.: Condens. Matter, 24 (2012) 175002.

[33] S. Anantharaj, S. Kundi, Do the Evaluation Parameters Reflect Intrinsic Activity of Electrocatalysts in Electrochemical Water Splitting?, ACS Energy Lett., 4 (2019) 1260-1264.
[34] Y. Zhu, W. Zhou, Y. Chen, J.C. Yu, M. Liu, Z. Shao, A High-Performance Electrocatalyst for Oxygen Evolution Reaction: LiCo0.8 Fe0.2 O2, Adv. Mater., 27 (2015) 7150.
[35] C.T. Moi, S. Bhwmick, T.K. Sahu, M. Qureshi, Electrocatalytic oxygen evolution surpassing benchmark RuO2 using stable, noble metal free vanadium doped hematite co-modified by NiFe Layered Double Hydroxide, Electrochim. Acta, 370 (2021) 137726.
[36] J. Wang, K. Wang, F.-B. Wang, X.-H. Xia, Bioinspired copper catalyst effective for both reduction and evolution of oxygen, Nat. Commun., 5 (2014) 5285.
[37] M. Li, Y. Xiong, X.-W. Liu, X. Bo, Y. Zhang, C. Han, L. Guo, Facile synthesis of electrospun MFe2O4 (M = Co, Ni, Cu, Mn) spinel nanofibers with excellent electrocatalytic properties for oxygen evolution and hydrogen peroxide reduction, Nanoscale, 7 (2015) 8920.
[38] H. Zhang, Z. Zhang, N. Li, W. Yan, Z. Zhu, Cu2O@C core/shell nanoparticle as an electrocatalyst for oxygen evolution reaction, J. Catal., 352 (2017) 239-245.
[39] T.N. Huan, G. Rousse, S. Zanna, I.T. Lucas, X. Xu, N. Menguy, V. Mougel, M. Fontecave, A Dendritic Nanostructured Copper Oxide Electrocatalyst for the Oxygen Evolution Reaction., Angew. Chem. Int. Ed., 56 (2017) 4792.
[40] J.-L. Bredas, Mind the gap! , Mater. Horizon, 1 (A014) 17–19.
[41] L. Wang, D. Lv, Z. Yue, H. Zhu, L. Wang, D. Wang, X. Xu, W. Hao, S.X. Dou, Y. Du, Promoting photoreduction properties via synergetic utilization between plasmonic effect and highly active facet of BiOCl, Nano Energy, 57 (2019) 398-404.
[42] T.e.a. 2010), DOI.

Plasmon-enhanced Electrocatalytic Activity of Gold Nanoparticles/Cu_2O Nanocrystals for Oxygen Evolution Reaction in Alkaline Media